Tellus (2001), 53A, 279–299
Printed in UK. All rights reserved

TELLUS
ISSN 0280–6495

A time-split, forward-backward numerical model for solving a nonhydrostatic and compressible system of equations

By WU-RON HSU[1]* and WEN-YIH SUN[2], [1]*Department of Atmospheric Sciences, National Taiwan University, 1, Roosevelt Road Sec. 4, Taipei, Taiwan 106;* [2]*Department of Earth and Atmospheric Science, Purdue University, 1397 Civil Engineering Building, West Lafayette, IN 47907, USA*

(Manuscript received 4 February 2000; in final form 6 October 2000)

ABSTRACT

In this paper, we present a numerical procedure for solving a 2-dimensional, compressible, and nonhydrostatic system of equations. A forward-backward integration scheme is applied to treat high-frequency and internal gravity waves explicitly. The numerical procedure is shown to be neutral in time as long as a Courant–Friedrichs–Lewy criterion is met. Compared to the leap-frog-scheme most models use, this method involves only two time steps, which requires less memory and is also free from unstable computational modes. Hence, a time-filter is not needed. Advection and diffusion terms are calculated with a time step longer than sound-wave related terms, so that extensive computer time can be saved. In addition, a new numerical procedure for the free-slip bottom boundary condition is developed to avoid using inaccurate one-sided finite difference of pressure in the surface horizontal momentum equation when the terrain effect is considered. We have demonstrated the accuracy and stability of this new model in both linear and nonlinear situations. In linear mountain wave simulations, the model results match the corresponding analytical solution very closely for all three cases presented in this paper. The analytical streamlines for uniform flow over a narrow mountain range were obtained through numerical integration of Queney's mathematical solution. It was found that Queney's original diagram is not very accurate. The diagram had to be redrawn before it was used to verify our model results. For nonlinear tests, we simulated the famous 1972 Boulder windstorm and a bubble convection in an isentropic enviroment. Although there are no analytical solutions for the two nonlinear tests, the model results are shown to be very robust in terms of spatial resolution, lateral boundary conditions, and the use of the time-split scheme.

1. Introduction

Nonhydrostatic numerical models are required for simulations of atmospheric systems with a small spatial scale, such as convective clouds, mountain waves excited by small-scale mountains and many local circulation systems. There are two major types of nonhydrostatic models categorized by the way in which the pressure field is calculated (Ikawa, 1988). One type is the anelastic model (for example, Ogura and Phillips, 1962; Clark, 1977; Smolarkiewicz and Margolin, 1997) which filters out sound waves in its model formulation equations. Although anelastic models appear to be very efficient for allowing very long integration time steps, obtaining a converged solution for pressure can be quite time consuming when large numbers of grid points are used. In addition, when a coordinate transformation is present, the Poisson solution procedure can be quite complicated (Durran and Klemp, 1983). Another type of

* Corresponding author.
e-mail: hi@hi.as.ntu.edu.tw

nonhydrostatic model is the compressible model. Compressible models solve sound waves despite their limited impact on most atmospheric systems. The integrating time step is very short due to the treatment of the fast-propagating sound waves, but the pressure field can be directly integrated or diagnosed indirectly through the integrated density field. With the advancement of computer technology in recent years, many investigators are choosing to develop or use a compressible nonhydrostatic model as their research tool.

In order to save computing time, an implicit scheme is often used in compressible models. Tapp and White (1976) and Carpenter (1979) treated the terms related to sound waves implicitly in both the horizontal and vertical directions. Tanquay et al. (1990), Cullen (1990) and Pinty et al. (1995) chose to apply an implicit scheme to both sound waves and gravity waves. The use of an implicit scheme, however, still leads to a complicated Helmholtz-type of equation for the pressure field as in an anelastic model. In addition, very extensive computer memory is required for storing a large number of coordinate transformation coefficients for solving the pressure equation. Perhaps, the most common approach is the use of an implicit scheme only in the vertical direction. In this approach, the vertically propagating sound waves are treated efficiently while the horizontal waves are solved explicitly, such as in Klemp and Wilhelmson (1978), Durran and Klemp (1983), Regional Atmospheric Modeling System (RAMS, Pielke et al., 1992), Pennsylvania State University-National Center for Atmospheric Research Mesoscale Model Version 5 (PSU-NCAR MM5, Dudhia, 1993), and Coupled Ocean/Atmosphere Mesoscale Prediction System (COAMPS, Hodur, 1997). This approach is very attractive, since the 1-dimensional (vertical) Helmholtz-type elliptic equation can be solved easily through a tri-diagonal matrix. This approach, however, may encounter instability problems for very steep mountain cases, or motions with compatible horizontal and vertical spatial scales (Ikawa, 1988; Sun, 1980; Steppeler, 1995).

In this paper, we present an explicit approach to solve a fully compressible, nonhydrostatic system of equations. This approach appears to be inefficient, but we will show that it is simple, memory saving, versatile, and accurate even for high frequency waves. The efficiency problem can be amended by the use of a time-split scheme. In addition, an explicit algorithm is particularly suited to run on parallel computers (processors). A lot of computer time can be saved by using a parallel computer.

A forward-backward procedure was developed for treating both sound waves and gravity waves. Since the forward-backward scheme is a two-level scheme and prognostic variables are immediately replaced during integration, it requires only 50% of the memory space compared to a three-level (at least two levels are required to be saved in memory) centered different scheme as used in most models. This method is shown to be neutral with respect to linear sound waves and internal gravity waves. Furthermore, there is no computational mode produced by this time integration procedure. There is, therefore, no need to impose a time filter as required in a leapfrog scheme. The amount of artificial smoothing imposed in a finite-difference model is then reduced and may lead to a more accurate solution.

Our method was validated by comparing the model results with the analytical solution for linear, dry mountain waves in Sections 3 through 5. The three different cases chosen for simulation are nonhydrostatic, hydrostatic and trapped mountain waves, respectively in each section. Simulations of the 11 January 1972 Boulder windstorm in Section 6 and bubble convection in Section 7 show the model's capacity in non-linear situations. Concluding remarks are presented in the last section of the paper.

2. Numerical method

The numerical method is an extension of the Purdue mesoscale model (PMM) (Chern, 1994; Hsu and Sun, 1994) which is a hydrostatic model. The original PMM employs a forward-backward time integration scheme. The new model presented in this paper builds an additional forward-backward procedure for treating sound waves. The vertical coordinate system and the model equations are similar to those in the original model (Sun and Hsu, 1988), with some necessary changes made for the new model.

2.1. Terrain following vertical coordinate

The vertical coordinate σ is defined as:

$$\sigma = \frac{p_0(z) - p_0(z_{\text{top}})}{p_0(z_{\text{surface}}) - p_0(z_{\text{top}})} = \frac{p_0(z) - p_0(z_{\text{top}})}{p^*}, \quad (2.1)$$

where p_0, pressure of a reference atmosphere, is strictly a function of height. Although this vertical coordinate appears to be a σ-pressure coordinate, as used in many hydrostatic models, the pressure in (2.1) is not a function of time. The position of each grid point is fixed in time as in most of the existing nonhydrostatic models. The model employs, strictly speaking, a σ–z coordinate. This arrangement is confusing, but convenient in terms of enabling the two models (the new model and PMM) to share many source code modules. Dudhia (1993) used this procedure to extend the PSU-NCAR MM4 into a nonhydrostatic model.

2.2. Model equations

The present model is 2-dimensional. The Coriolis force and moisture effects are ignored in this paper, but they can be incorporated easily into the model. The momentum, mass conservation, and thermodynamic equations are in the following formats:

$$\frac{\partial \theta}{\partial t} = -u\frac{\partial \theta}{\partial x} - \dot{\sigma}\frac{\partial \theta}{\partial \sigma} + D_\theta, \quad (2\cdot2)$$

$$\frac{\partial \rho}{\partial t} + \rho\left[\frac{\partial u}{\partial x} + \left(\frac{\partial \sigma}{\partial x}\right)_z \frac{\partial u}{\partial \sigma} + \frac{\partial \sigma}{\partial z}\frac{\partial w}{\partial \sigma}\right] = -u\frac{\partial \rho}{\partial x} - \dot{\sigma}\frac{\partial \rho}{\partial \sigma}, \quad (2.3)$$

$$\frac{\partial u}{\partial t} + \frac{1}{\rho}\left[\frac{\partial p'}{\partial x} + \left(\frac{\partial \sigma}{\partial x}\right)_z \frac{\partial p'}{\partial \sigma}\right] = -u\frac{\partial u}{\partial x} - \dot{\sigma}\frac{\partial u}{\partial \sigma} + D_u, \quad (2\cdot4)$$

$$\frac{\partial w}{\partial t} + \frac{1}{\rho}\frac{\partial \sigma}{\partial z}\frac{\partial p'}{\partial \sigma} = -u\frac{\partial w}{\partial x} - \dot{\sigma}\frac{\partial w}{\partial \sigma} - \frac{\rho - \rho_0}{\rho} g + D_w, \quad (2\cdot5)$$

where

$$p' = \left(\frac{R_d}{p_{00}^{R_d/c_p}}\rho\theta\right)^{c_p/c_v} - p_0(z) \quad (2.6)$$

and

$$\dot{\sigma} = \frac{\partial \sigma}{\partial z} w + \left(\frac{\partial \sigma}{\partial x}\right)_z u. \quad (2.7)$$

In the above equations, u and w are the horizontal and vertical velocity components, ρ the density, θ the potential temperature, R_d the gas constant for dry air, c_p and c_v the specific heat of the dry air at constant pressure and volume, respectively. The vertical velocity in the transformed σ coordinate is $\dot{\sigma}$. The D's are contributions from subgrid scale mixing, other sources and sink terms are ignored in the model at this time. The diffusion terms were only calculted for the nonlinear tests in Sections 6 and 7, since there is no turbulence generated in all linear cases presented in the paper.

It should be noted that we have chose density, instead of pressure (or π), as a prognostic variable in this new model. The change in the pressure time rate is affected by the diabatic heating term, dh/dt, while the heating term does not appear explicitly in the prognositc equation for density. The diabatic effect on pressure is accounted for at the time pressure is retrieved through the equation of state. Thus, the prediction equation for density has the advantage of taking a simpler form than a pressure equation, when this effect is considered. Pressure perturbation calculated diagnostically through (2.6) is then used to calculate the pressure gradient force terms in momentum equations as most numerical models do.

2.3. Finite differencing scheme

The compressible system (2.2)–(2.6) includes fast propagating sound waves. This imposes a severe limit to the time step which can be used in explicit numerical integration schemes. In order to amend this problem, we employed a time splitting (Gadd, 1978) technique. The integration was divided into three stages, in which the length of the time step varied according to the corresponding physical time scale of the terms calculated. The three stages are advection, high-frequency-wave and diffusion stages.

(1) *THE ADVECTION STAGE*

The first and second terms on the right hand side of the equal sign of (2.2)–(2.5) are advection terms. They are all calculated in a forward manner with a time step denoted by Δt. The changes in prognostic variables due to advection terms, as denoted in the following equations, are saved into the computer memory before they are accumulated in pieces with several shorter time steps later in the high-frequency-wave stage.

$$\Delta\psi_{\text{adv}} = \Delta t\left(-u\frac{\partial\psi}{\partial x} - \dot{\sigma}\frac{\partial\psi}{\partial\sigma}\right), \tag{2.8}$$

where ψ can be any one of the four prognostic variables. The algorithm follows Sun (1993) for the horizontal advection term in (2.8). This advection scheme is more accurate than the Crowley 4th order scheme (Crowley, 1968). The algorithm for integration of the terms involving vertical motion for mountain wave simulations in Sections 3–6 is the Crowley 2nd order scheme. The numerical results for those tests are not sensitive to the accuracy of the vertical advection term. The advection time step that can be used in the model is restricted by the split ratio between the advection time step and the high-frequencey-wave time-step, in addition to the advection speed and gravity wave phase speed. As we will show later that we cannot apply a very large split ratio without sacrificing accuracy of the simulation.

(2) *THE HIGH-FREQUENCY-WAVE STAGE*
The terms that are responsible for rapid sound wave propagation are isolated on the left-hand side of eqs. (2.2), (2.4), and (2.5). They are integrated separately with a smaller time step (Δt_s in the following equations) than that used for advection and diffusion processes.

The forward part of the integration involves the changes in potential temperature and density:

$$\frac{\theta^{n+1}-\theta^n}{\Delta t_s} = \frac{1}{\Delta t}\Delta\theta_{\text{adv}}, \tag{2.9}$$

$$\frac{\rho^{n+1}-\rho^n}{\Delta t_s} = -\rho^n\left[\frac{\partial u}{\partial x} + \left(\frac{\partial u}{\partial x}\right)_z\frac{\partial u}{\partial\sigma} + \frac{\partial\sigma}{\partial z}\frac{\partial w}{\partial\sigma}\right]^n + \frac{1}{\Delta t}\Delta\rho_{\text{adv}}, \tag{2.10}$$

$$p'^{n+1} = \left(\frac{R_d}{p_{00}^{R_d/c_p}}\rho^{n+1}\theta^{n+1}\right)^{c_p/c_v} - p_0(z). \tag{2.11}$$

Momentum fields are integrated in a backward manner as:

$$\frac{u^{n+1}-u^n}{\Delta t_s} = -\frac{1}{\rho^{n+1}}\left[\frac{\partial p'}{\partial x} + \left(\frac{\partial\sigma}{\partial x}\right)_z\frac{\partial p'}{\partial\sigma}\right]^{n+1} + \frac{1}{\Delta t}\Delta u_{\text{adv}}, \tag{2.12}$$

$$\frac{w^{n+1}-w^n}{\Delta t_s} = -\frac{1}{\rho^{n+1}}\left(\frac{\partial\sigma}{\partial z}\frac{\partial p'^{n+1}}{\partial\sigma}\right) - \frac{\rho^{n+1}-\rho_0(z)}{\rho^{n+1}}g + \frac{1}{\Delta t}\Delta w_{\text{adv}}. \tag{2.13}$$

Superscript, n, denotes the time level. The numerical procedure can be viewed from the linear perspective that the forward-backward scheme is used to treat both high-frequency waves and internal gravity waves. For high-frequency waves, the divergence term is forward and the pressure gradient force terms are backward. For the relatively slow varying gravity waves, the vertical advection terms in (2.9) and (2.10), which generate negative buoyancy in a stratified atmosphere, are integrated in a forward manner, while the buoyancy and pressure gradient force terms in (2.12) and (2.13) are integrated backward. A longer time step can be used for the forward integration on vertical advection terms, but several succeeding shorter steps must be repeated for integration on momentum fields because high-frequency waves are also treated in the system. We shall show in the next subsection that this algorithm is neutral in time with respect to both linear sound waves and linear internal gravity waves as long as a Courant–Friedrichs–Lewy (CFL) condition is met. More properties of the numerical method are also discussed in the next subsection.

All spatial differences are centered differences. Fig. 1 shows the staggered grid structure used in the model. All thermodynamic variables are located in the same position, while u and w are staggered with the thermodynamic variables in the x and z directions, respectively. This arrangement is best for treating the divergence term in the density equation, that is, (2.10). The vertical velocity at the lower boundary, however, is located at the same location as the thermodynamic variables.

(3) *THE DIFFUSION STAGE*
Turbulence parameterization is modified from Durran and Klemp (1983). It is a first-order closure scheme, where mixing coefficients are functions of the Richardson number and grid point intervals. We used a simple forward method to account for all of the D terms in the model equations. The time step (Δt_b) is longer than the advection time step (Δt) for the Boulder windstorm and bubble convection simulations in Sections 6

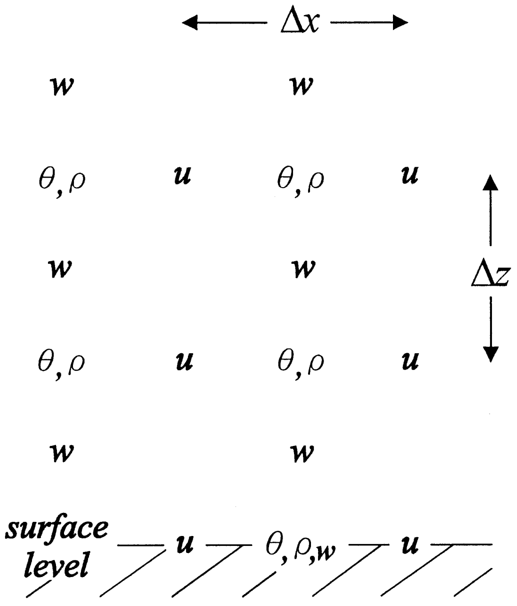

Fig. 1. Staggered grid system used in the model.

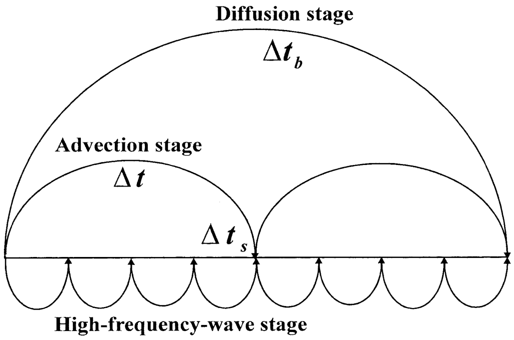

Fig. 2. Schematic diagram of the model time-split method.

and 7. As a summary, Fig. 2 demonstrates how the time integration is broken down into the three stages in the case of $\Delta t_b = 2\,\Delta t$, and $\Delta t = 4\,\Delta t_s$.

2.4. *Linear stability analysis*

We can linearize the governing eqs. (2.2)–(2.6) as follows (neglecting the diffusion terms)

$$\frac{\partial\theta'}{\partial t} + w'\frac{\partial\theta'}{\partial z} = 0, \tag{2.14}$$

$$\frac{\partial\rho'}{\partial t} + \rho_0\left(\frac{\partial u'}{\partial x} + \frac{\partial w'}{\partial z}\right) + w'\frac{\partial\rho_0}{\partial z} = 0, \tag{2.15}$$

$$\rho' = \frac{p'}{c^2} - \frac{\rho_0}{\theta_0}\theta', \tag{2.16}$$

$$\frac{\partial u'}{\partial t} + \frac{1}{\rho_0}\frac{\partial p'}{\partial x} = 0, \tag{2.17}$$

$$\frac{\partial w'}{\partial t} + \frac{1}{\rho_0}\frac{\partial p'}{\partial z} + g\frac{\rho'}{\rho_0} = 0. \tag{2.18}$$

In these equations, primes are deviations from basic state variables (with subscript "0") which are functions of height only and $c^2 = \sqrt{(c_p/c_v)R_d T}$. The basic state wind components, u_0 and w_0, are both assumed to be zeroes for simplicity. Substituting (2.16) into (2.18) and changing the definition of variables with $\hat{u} = \sqrt{\rho_0}u'$, $\hat{w} = \sqrt{\rho_0}w'$, $\hat{p} = (1/\sqrt{\rho_0})p'$, and $\hat{\theta} = (\sqrt{\rho_0}/\theta_0)\theta'$, we have:

$$\frac{\partial\hat{\theta}}{\partial t} + \hat{w}S_0 = 0, \tag{2.19}$$

$$\frac{1}{c^2}\frac{\partial\hat{p}}{\partial t} + \frac{\partial\hat{u}}{\partial x} + \frac{\partial\hat{w}}{\partial z} + \left(S_0 + \frac{R_0}{2}\right)\hat{w} = 0, \tag{2.20}$$

$$\frac{\partial\hat{u}}{\partial t} + \frac{\partial\hat{p}}{\partial x} = 0, \tag{2.21}$$

$$\frac{\partial\hat{w}}{\partial t} + \frac{\partial\hat{p}}{\partial z} + \left(\frac{g}{c^2} + \frac{R_0}{2}\right)\hat{p} - g\hat{\theta} = 0, \tag{2.22}$$

where

$$S_0 \equiv \frac{1}{\theta_0}\frac{\partial\theta_0}{\partial z}, \qquad R_0 \equiv \frac{1}{\rho_0}\frac{\partial\rho_0}{\partial z}.$$

Note that the linearized equations are more simplified due to the change in variables, this is an important step to aid subsequent analysis. We then followed the standard Von Neumann stability analysis by letting

$$\begin{bmatrix}\hat{\theta}\\ \hat{p}\\ \hat{u}\\ \hat{w}\end{bmatrix}(j\Delta x, k\Delta z, n\Delta t) = \begin{bmatrix}\Theta\\ P\\ U\\ W\end{bmatrix}\lambda^n e^{i(lj\Delta x + mk\Delta z)}, \tag{2.23}$$

The perturbation fields are discretized and the indices for addressing the grid points are j, k, and n in the x direction, z direction and time, respectively. The wave numbers in the x and z

directions are l and m, respectively. The amplification factor for testing the stability of a numerical method is λ.

Our newly developed numerical method presented in Subsection 2.3, can now be tested for the linear, non-spliting situation by substituting (2.23) into (2.19)–(2.22) with forward difference for $\partial\hat{\theta}/\partial t$ and $\partial\hat{p}/\partial t$, backward integration for $\partial\hat{u}/\partial t$ and $\partial\hat{w}/\partial t$. All spatial derivatives are replaced by centered differences with a half of grid distance on either side because of the staggered grid structure (Fig. 1). The set of linear equations becomes

$$\left(\frac{\lambda-1}{\Delta t}\right)\Theta + S_0 W = 0, \tag{2.24}$$

$$\left(\frac{\lambda-1}{\Delta t}\right)\frac{1}{c^2}P + iXU + iZW + \Gamma_0 W = 0, \tag{2.25}$$

$$\left(\frac{\lambda-1}{\Delta t}\right)U + iX\lambda P = 0, \tag{2.26}$$

$$\left(\frac{\lambda-1}{\Delta t}\right)W + iZ\lambda P - \Gamma_0\lambda P - g\lambda\Theta = 0, \tag{2.27}$$

where

$$X \equiv \frac{\sin(l\Delta x/2)}{\Delta x/2}, \qquad Z = \frac{\sin(m\Delta z/2)}{\Delta z/2},$$

$$\Gamma_0 = S_0 + R_0/2.$$

Note that the coefficient, $g/c^2 + R_0/2$, in (2.22) is replaced by $-\Gamma_0$ in (2.27), since it can be shown through the hydrostatic equation of the basic state that

$$S_0 = -g/c^2 - R_0. \tag{2.28}$$

The amplification factor, λ, can be solved by setting the determinant of the coefficient matrix of (2.24)–(2.27) to zero. Thus, we have

$$\frac{1}{c^2}(\lambda-1)^4 + \Delta t^2\left(X^2 + Z^2 + \Gamma_0^2 + \frac{gS_0}{c^2}\right)\lambda(\lambda-1)^2 + \Delta t^4 g S_0 X^2\lambda^2 = 0. \tag{2.29}$$

In order to understand the stability properties of our numerical method, we can consider two special cases of (2.29). If gS_0 equals to zero, (2.29) becomes

$$\frac{1}{c^2}(\lambda-1)^2 + \Delta t^2(X^2 + Z^2 + \Gamma_0^2)\lambda = 0. \tag{2.30}$$

This equation is related to pure sound waves. Our numerical method is neutral ($|\lambda| = 1$) as long as

$$\Delta t < 2\sqrt{\frac{1}{c^2(X^2 + Z^2 + \Gamma_0^2)}}. \tag{2.31}$$

If $1/c^2$ terms are dropped in (2.29), we obtain the solution for pure internal gravity waves by solving

$$(X^2 + Z^2 + \Gamma_0^2)(\lambda-1)^2 + \Delta t^2 g S_0 X^2\lambda = 0, \tag{2.32}$$

The forward-backward algorithm is again neutral as long as

$$\Delta t < 2\sqrt{\frac{X^2 + Z^2 + \Gamma_0^2}{gS_0X^2}}. \tag{2.33}$$

The last equation is the same result as in Sun (1980) in which the stability criterion of a forward-backward scheme was obtained for a set of anelastic equations. As for general cases of internal gravity waves mixed with sound waves, we can still solve the 4th-order polynomial (2.29), since all coefficients are real numbers. The stability of the numerical method depends on basic state parameters, wave numbers and the grid interval. Fig. 3 demonstrates the magnitude of the amplification factor as a function of Δt for the case of $l = \pi/\Delta x$, $m = \pi/\Delta z$ (most restrictive wave number in terms of the time step that can be used in the model). Four roots of (2.29) correspond to two slow and two fast physical modes of (2.14)–(2.18). With a small Δt, all modes are neutral as the

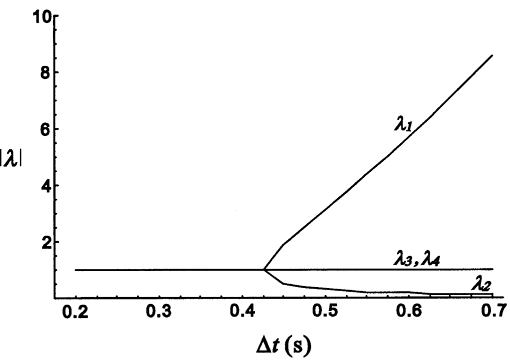

Fig. 3. Magnitude of the amplification factors for the model forward-backward scheme in the linear case of $c = 330\ \mathrm{m\ s^{-1}}$, $gS_0 = 10^{-4}\ \mathrm{s^{-2}}$, $l = \pi/\Delta x$, $m = \pi/\Delta z$, and $\Delta x = \Delta z = 200$ m. These three lines correspond to four roots of (2.29) and the magnitudes of the two slow modes are the same (=1) for the range of Δt presented in the figure.

physical solution. From the stability analysis, we can conclude that the numerical method is neutral in time with respect to both linear sound waves and internal gravity waves as long as the CFL condition is met. It should be noted that our analysis is performed for an inviscid flow. In our simulations, a time step slightly longer than the critical time step according to (2.29) is used because the model has weak smoothing in space.

Since this procedure is neutral and does not produce unstable computational modes, as a leapfrog scheme does (Skamarock and Klemp, 1992), there is no need to impose any time smoother or filter during the entire course of integration. In addition, since the method is very stable, we have not imposed any smoothing in space on prognostic variables as well for linear mountain wave simulations in Sections 3–5. Only for the highly nonlinear 1972 Boulder windstorm simulation in Section 6 and the nonlinear bubble simulation in Section 7, was very slight smoothing in space applied to prognostic variables to filter out the aliasing errors generated by nonlinear terms. Without artificial smoothing in time and space, numerical results should be very reliable. The test cases in this paper demonstrate the validity of our method.

2.5. *Boundary conditions*

The open lateral boundary condition in Sun et al. (1991) was used. In addition, we added 50-grid buffer zones (Rayleigh damping) on each lateral boundary to avoid wave reflection by the artificial boundaries. The sponge coefficient for lateral boundaries is a linear function. It is the largest right at the lateral boundary and diminishes linearly toward the inner domain within the 50-grid buffer zones. The top boundary is also a sponge layer. It is very deep with at least 40 levels in each vertical column. As a lateral boundary buffer, the damping coefficient decreases linearly from the top toward the inner domain within the damping layer.

A free-slip condition was used at the ground surface. Since the ground is a material surface, we require that the normal velocity vanish at the surface:

$$\dot{\sigma} = \frac{\partial \sigma}{\partial z} w + \left(\frac{\partial \sigma}{\partial x}\right)_z u = 0, \qquad \text{for } \sigma = 0. \tag{2.34}$$

We tried several extrapolation techniques to obtain u at the surface, but always failed to get a reasonable surface pressure distribution in both the linear and nonlinear mountain wave simulations. We then decided to integrate u at the surface, and then solve w through (2.34). The surface grid arrangement described earlier is related to the bottom boundary condition. However, it was found that the model becomes unstable for the windstorm simulation, if we integrate (2.4) directly. The problem lies in the coordinate transformation term related to $\partial p'/\partial\sigma$. This expression can only be evaluated through a non-centered finite difference method, since there is no p' value available beneath the ground surface. The error can be very large near a mountain. We therefore derived another prognostic equation for u at the ground surface to avoid this problem. By letting $\dot{\sigma}$ equal zero, (2.4) and (2.5) become:

$$\frac{\partial u}{\partial t} + \frac{1}{\rho}\left[\frac{\partial p'}{\partial x} + \left(\frac{\partial \sigma}{\partial x}\right)_z \frac{\partial p'}{\partial \sigma}\right] = -u\frac{\partial u}{\partial x}, \tag{2.35}$$

$$\frac{\partial w}{\partial t} + \frac{1}{\rho}\frac{\partial \sigma}{\partial z}\frac{\partial p'}{\partial \sigma} = -u\frac{\partial w}{\partial x} - \frac{\rho'}{\rho} g, \qquad \text{for } \sigma = 0. \tag{2.36}$$

Combining (2.35) and (2.36) by canceling $\partial p'/\partial\sigma$, we obtained another form of the horizontal momentum equation for the ground surface with the aid of (2.34):

$$\begin{aligned}\frac{\partial u}{\partial t} &+ \frac{\left(\frac{\partial \sigma}{\partial z}\right)^2}{\left(\frac{\partial \sigma}{\partial z}\right)^2 + \left(\frac{\partial \sigma}{\partial x}\right)_z^2}\frac{1}{\rho}\frac{\partial p'}{\partial x} \\ &= -u\frac{\partial u}{\partial x} + \frac{\left(\frac{\partial \sigma}{\partial x}\right)_z\left(\frac{\partial \sigma}{\partial z}\right)}{\left(\frac{\partial \sigma}{\partial z}\right)^2 + \left(\frac{\partial \sigma}{\partial x}\right)_z^2}\frac{\rho'}{\rho} g \\ &\quad + u^2\left[\left(\frac{\partial \sigma}{\partial x}\right)_z^2 \frac{\partial \ln\left(\left|\frac{\partial \sigma}{\partial z}\right|\right)}{\partial x} - \frac{1}{2}\frac{\partial \left(\frac{\partial \sigma}{\partial x}\right)_z^2}{\partial x}\right] \Bigg/ \\ &\quad \left[\left(\frac{\partial \sigma}{\partial z}\right)^2 + \left(\frac{\partial \sigma}{\partial x}\right)_z^2\right].\end{aligned} \tag{2.37}$$

The last term of (2.37) comes from the advection term of (2.36). Although this new form of momentum equation for the bottom surface looks complicated, the coefficients regarding σ are constants. They can be stored into the computer memory in the beginning of the simulation. Eq. (2.37) can then be evaluated quite accurately with a centered difference method, since all spatial finite differences are in the x-direction. The model is apparently very sensitive to lower boundary conditions. The magnitude of the pressure-gradient-force term of (2.37) is smaller than the original form in (2.35), since the additional coefficient is always less than 1 with a sloping terrain. In addition, the advection and buoyancy terms have a stabilizing effect. Thus, this new form of the momentum equation stabilizes the model and provides a more accurate simulation result, especially for nonlinear situations.

3. Simulation of nonhydrostatic linear mountain waves

3.1. *Anelastic analytical solution*

The new numerical procedure was tested against an analytical solution for linear mountain waves. Queney (1948) found anelastic solutions for uniform flow over a "bell-shaped" ridge of the form:

$$h = h_m \Big/ \left[1 + \left(\frac{x}{a} \right)^2 \right] = h_m a \int_0^\infty e^{-ka} \cos kx \, dk. \tag{3.1}$$

where h is terrain height, h_m the maximum terrain height, a the half width, which is a measure of the horizontal length scale of the mountain. The background environment of the waves is uniform stratification with a free-slip bottom surface. The bell-shaped ridge is convenient for study because of the simple form of its Fourier transform in the above equation. The response to airflow can be found by taking an appropriate combination of the solutions for all of the sinusoidal topography components.

We have chosen the case of uniform wind speed $U = 10\ \mathrm{m\ s^{-1}}$, the Brunt–Väisälä frequency $N = 0.01\ \mathrm{s^{-1}}$, $a = 1000$ m for comparison. Gill (1982) categorized $a \sim U/N$ as belonging to the non-hydrostatic wave regime. The anelastic solution of the streamline vertical displacement is:

$\zeta =$ real part of

$$\sqrt{\frac{\rho_0}{\rho}} (k_s a) h_s \int_0^\infty \exp i(x't + z'\sqrt{1 - t^2}) \, dt, \tag{3.2}$$

where ρ is density, ρ_0 the surface air density, $x' = k_s(x + ia)$, $z' = k_s z$, $k_s = N/U$, and $i = \sqrt{-1}$. Queney (1948) calculated the solution by solving the Fourier Bessel expansion of the above integral without the help of the present day advanced computer. Fig. 1 of his paper plots the streamlines and the ground surface pressure distribution. The classical diagram also appeared as Fig. 54-1 in Gill (1982) and Fig. 5 in Smith (1979). We found, however, that this diagram is not very accurate and the solution has to be recalculated before it is used to validate our model result.

We recalculated the solution by direct integration of (3.2) numerically using Simpson's 1/3 rule (evenly spaced functional values are summed up by weighting coefficients of 1/3, 4/3, 2/3, 4/3, 2/3, ...). The increment of the dummy variable, Δt (not time step), is $1/200\ \mathrm{m^{-1}}$, and the upper limit of the numerical integration is $t = 10\ \mathrm{m^{-1}}$. The result is plotted in Fig. 4. We verified this result by comparing it with the result of doubling Δt and halving the upper limit to make sure that our result is very accurate. Indeed almost no difference appears for these two solutions. The integration increment and upper limit of t that we used are adequate.

Although the general pattern of the displacement looks similar for Queney's original diagram and Fig. 4, there are discrepancies in many places. First of all, even though the wave energy is mainly concentrated in the downstream region of the mountain, the displacement is far from zero at 6 km upstream from the mountain as in Queney's diagram. Secondly, Queney's solution is too strong (over 30% in some places) below the 3 km level and a little bit weak in the upper levels. The most significant difference between the two diagrams is the surface pressure distribution. Our calculated amplitude of the pressure deviation is more than twice as strong as Queney's. In addition, the surface pressure perturbation can be positive in the downstream region, but it is always negative in his figure. Since pressure is calculated through the vertical derivative of the displacement as in the following equation:

$$p' = \rho_0 U^2 \frac{\partial \zeta}{\partial z} \sim \rho_0 U^2 \frac{\Delta \zeta}{\Delta z}, \tag{3.3}$$

the requirement for accuracy of the displacement is very high. We used the displacements at the ground and 10 m levels to estimate the pressure

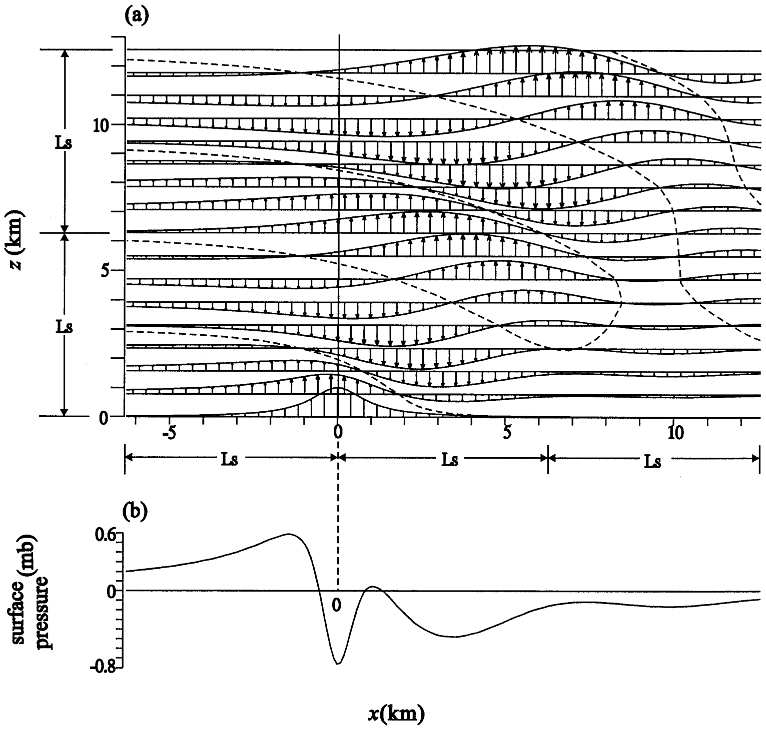

Fig. 4. Recalculated Queney's (1948) original solution for the perturbation produced by a narrow mountain range (half-width length of 1 km) in an unlimited stratified current ($U = 10$ m s^{-1}, $N = 0.01$ s^{-1}). L_s is $2\pi U/N$. (a) Vertical displacement of the streamlines. (b) Perturbation of pressure and longitudinal wind velocity at ground level. The analytical solution was obtained through direct integration of (3.2) with Simpson's 1/3 rule.

deviation in Fig. 4. Should we use the 200-m streamline displacement, the pattern would be like that of Queney's but with a larger amplitude. This may indicate that a very high resolution is required to obtain an accurate solution. It should be noted that Klemp and Lilly (1980) calculated the surface pressure distribution correctly a long time ago. The pressure curve for $aN/U = 1$ in their Fig. 5 supports our findings that the Queney solution is in error. Klemp and Lilly (1980) discussed the surface pressure character for a wide range of mountain widths, but did not note Queney's error and did not provide streamlines for the nonhydrostatic mountain waves.

3.2. *Model simulation*

In this simulation, the computational domain contains 341 points in the horizontal and 150 levels in the vertical direction. The top 60 levels constitute the absorption layer stated earlier. The grid interval is 200 m in the x-direction and approximately the same in the z-direction. Since our model is nonlinear, a very small mountain height ($h_m = 10$ m) is used for simulating linear mountain waves. The wave amplitude is later multiplied by 100 in order to compare it with the recalculated Queney's solution ($h_m = 1$ km) described in the last subsection. The mountain is placed in the center of the 68 by 30 km^2 domain. Time steps for the advection stage and high-frequency-wave stage are 3 and 0.5 s, respectively. Fig. 5 shows model streamline after 10 h of integration. The airflow actually already reached a steady state after 5 h. The recalculated Queney solution of Fig. 4 is repeated in Fig. 5 for comparison. The compressible numerical solution and the anelastic analytical solution are almost perfectly matched.

It is noted that the numerical model actually has verified the validity of the recalculated ana-

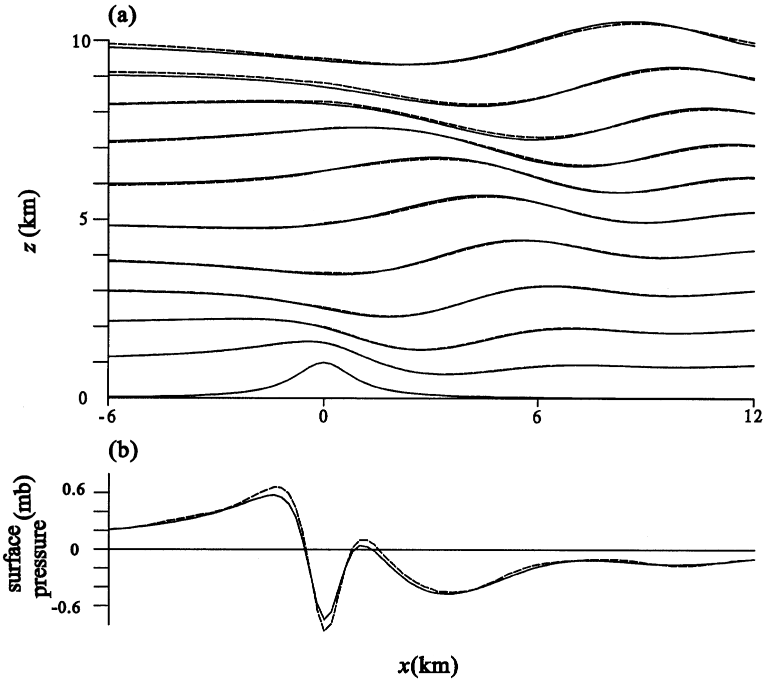

Fig. 5. (a) Streamlines and (b) surface pressure perturbation obtained from the analytical solution (solid lines) and by numerical simulation after 10 h with $\Delta t = 6\,\Delta t_s = 3$ s and $\Delta x = \Delta z = 200$ m (dashed lines) for mountain waves as in Fig. 4. We multiplied the magnitudes of model perturbations by 100 for comparison. As such they constitute a linear solution for a 1 km high mountain.

lytical solution. These two completely different approaches produce similar solutions, while the original Queney's pressure distribution is far apart from the two pressure curves in Fig. 5.

4. Simulation of hydrostatic linear mountain waves

One of the hydrostatic test cases presented in Durran and Klemp (1983) was performed using our model. This is also a test for uniform flow over a bell-shaped ridge. The half-width length is 10 km, which is much wider than the previous section. The background flow is an isothermal atmosphere with $U = 20$ m s^{-1} and $T = 250$ K. We used the same grid interval ($\Delta x = 2$ km, $\Delta z = 200$ m) and the same number (40) of nudging levels as in Durran and Klemp (1983).

The simulated streamlines (not shown) also match the corresponding analytical solution very well. We only presented vertical momentum flux profiles for two simulations with and without the time-split technique in Fig. 6. The numerical solutions again reached a steady state after long integration. Theoretically, the vertical momentum flux remains constant with height, since the mountain waves propagate upward without losing their energy in the linear condition. Our results show a nearly perfect flux profile from the surface up to 4 km (corresponding to nondimensional height, Nz/U, about 4 in Fig. 6) in height. As for the upper half of the domain, waves are artificially absorbed in the damping layer, and the calculated flux approaches zero with height. The numerical solution right beneath the damping layer is slightly off from the analytical value. The damping layer may have affected the numerical solution, as it is very difficult to impose a perfect upper boundary condition. The result from the no-time-split simulation is better than the time-split simulation.

Our results are quite consistent with Durran and Klemp (1983). It should be noted that the time step in our model is much shorter than their

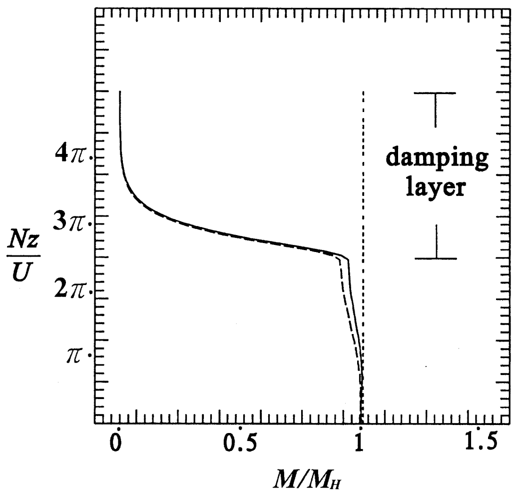

Fig. 6. Vertical flux of horizontal momentum ($M = \int \rho u'w' \, dx$), normalized by the analytical value, M_H, at nondimensional time $Ut/a = 60$ for simulation with time-split technique ($\Delta t = 6\,\Delta t_s = 3$ s) in dashed line and without time-split technique ($\Delta t = \Delta t_s = 0.5$ s) in solid line for hydrostatic mountain waves described in Section 4. The dotted line represents the analytical profile. M_H is $-(\pi/4)\rho_0 NUh^2$, in which $\rho_0 = 1.3937$ kg m^{-3}, $N = 0.019561$ s^{-1}, $U = 20$ m s^{-1} and $h_m = 1$ m. The value of surface density corresponds to $T = 250$ K and $p_0 = 1000$ hPa.

model. This is simply due to the nature of our model. There were very few assumptions in establishing this model, and the sound waves are explicitly resolved. Therefore, the model cannot be very efficient, and the applicability of the model is limited when Δx is much larger than Δz. Although our numerical method is designed to mainly focus on nonhydrostatic phenomena, it is, however, still accurate in this hydrostatic situation.

5. Simulation of linear trapped mountain waves

Another test case that can be of interest to validate a numerical method is the linear trapped mountain waves solved by Scorer (1949). Resonant waves develop near the ground surface downstream from a bell-shaped mountain in his two-layer model as long as the following Scorer condition is met:

$$l_1^2 - l_2^2 \geqslant \frac{\pi^2}{4H^2}, \tag{5.1}$$

where

$$l^2 = \frac{N^2}{\bar{u}^2} - \frac{d^2\bar{u}/dz^2}{\bar{u}}. \tag{5.2}$$

The symbols l_1 and l_2 denote the Scorer parameters of the lower and upper layers, respectively. They are uniform within each layer. The depth of the lower layer is H.

The solution for trapped waves can be evaluated by contour integration over a complex wave number plane (Scorer, 1949). We have again calculated the solution numerically using Simpson's 1/3 rule with a very fine resolution in wave number for the case of $l_1^2 = 10^{-6}$ m^{-2}, $l_2^2 = 1.5 \cdot 10^{-7}$ m^{-2}, $H = 3$ km, $a = 2.5$ km, $h_m = 1$ m and $\rho_0 = 1.16124$ kg m^{-3}. The value of ρ_0 corresponds to surface pressure at 1000 hPa and temperature 300 K.

Simulation of the trapped waves can be an interesting, but difficult, test for two reasons. First, a finite difference model cannot have a perfect two-layer structure. Two uniform layers with different Scorer parameters are apart by at least one vertical grid for a numerical model, instead of joining together in the theoretical model. In addition, the amplitude of the resonant waves in the analytical solution remains unchanged regardless how far downstream from the source of disturbance. Obviously, it is not possible to duplicate this behavior with a finite-difference model. However, we can test the accuracy of a numerical model by examining how much energy of the trapped waves can be retained far away from the mountain. Thus, the case is interesting in terms of validating a numerical model.

For simplicity, we used uniform mean wind (10 m s^{-1}) for both upper and lower layers in the simulation. The Scorer parameter defined in (5.2) would then be only a function of the Brunt–Väisälä frequency, N. N_1^2 and N_2^2 are 10^{-4} and 1.5×10^{-5} s^{-2}, respectively, to simulate two uniform layers of Scorer parameters. The surface pressure is 1000 hPa, temperature 300 K so that the surface density is the same as the analytical value described earlier. All background conditions are the same for the analytical solution and numerical solution, except that the two layers of different Scorer parameter for numerical solution is separated by one vertical grid ($\Delta z = 200$ m). The horizontal grid distance is also 200 m.

The simulated streamlines after 12 h match the analytical solution (Fig. 7) very closely. At that time, the numerical solution has already reached a steady state. But for vertical motion, the amplitude of the simulated lee waves deteriorates gradually downstream from the mountain (Fig. 8). Compared with the analytical vertical velocity (Fig. 9), the amplitude of the last cell with downward motion at around $x = 75$ km is

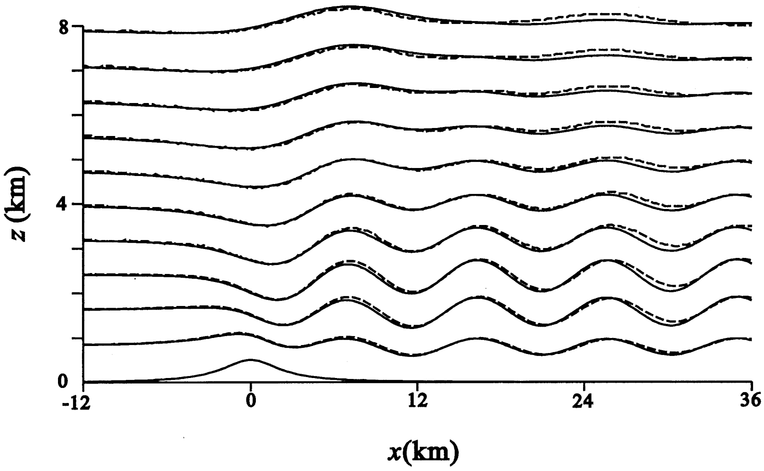

Fig. 7. Streamlines obtained from analytical solution (solid lines) and by numerical simulation after 10 h with $\Delta t = 4\,\Delta t_s = 2$ s (dashed lines) for trapped mountain waves described in Section 5. We amplified the vertical displacement of streamlines by 500 to show these two linear solutions. The center of the mountain is located at $x = 0$. We integrated Scorer's (1949) displacement equation with Simpson's 1/3 rule to obtain the analytical solution.

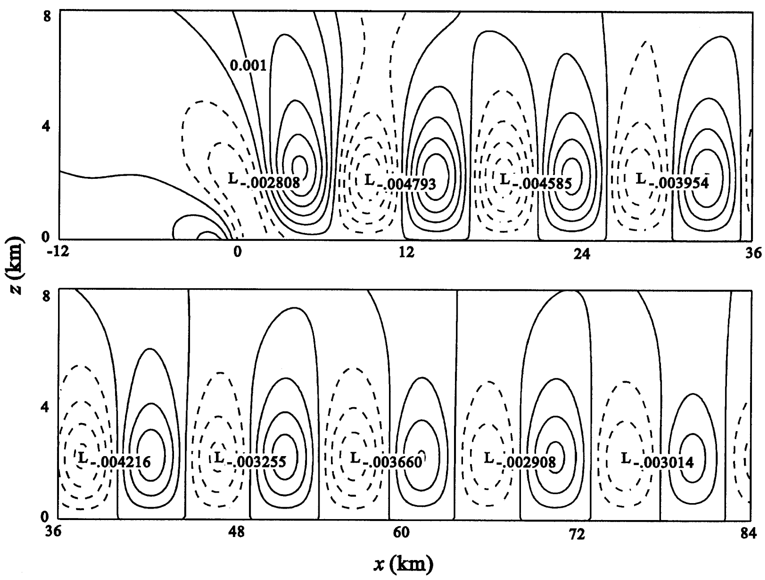

Fig. 8. Simulated vertical motion after 12 h for trapped mountain waves described in Section 5. Split scheme with $\Delta t = 4\,\Delta t_s = 2$ s was used. The contour interval is 0.001 m s^{-1}. Dashed lines are negative contours. The center of the mountain is located $x = 0$.

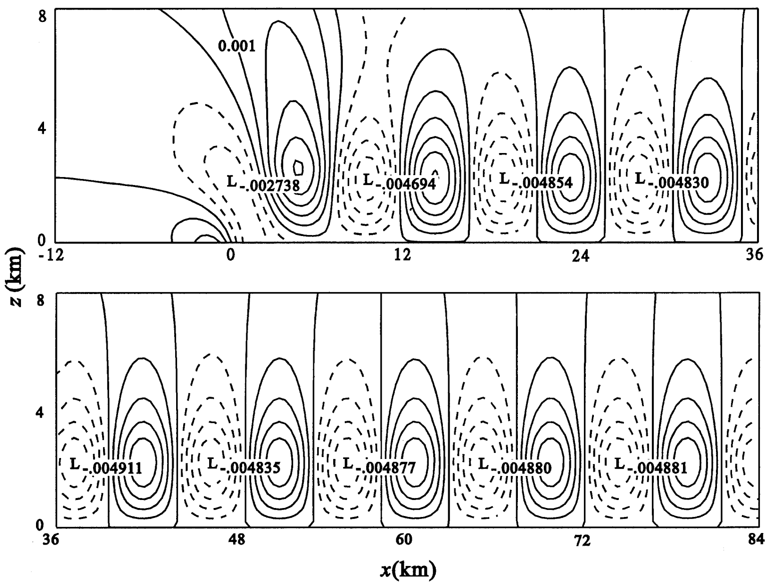

Fig. 9. Same as Fig. 8, except for Scorer's (1949) analytical solution obtained through using Simpson's 1/3 rule.

-0.003 m s^{-1}, which is only about 60% of the analytical value (-0.0049 m s^{-1}). It should be noted that the integrating domain is very large. The domain is from -62 to 134 km in the horizontal direction and 25 km (including an 8-km buffer zone) in the vertical direction. Durran and Klemp (1982) performed a similar test. We used a different wind profile from theirs. The analytical vertical motion is weaker in our case.

The model results presented in Figs. 7 and 8 were generated with the time-split technique. The advection time step is 4 times as large as the high-frequency-wave time step. We also tested the time-split effect again with a no-split simulation. All other conditions remain the same. The vertical motion field is presented in Fig. 10. The simulated lee waves deteriorate very little in this case. The amplitude of the cell at around $x = 75$ km (very far downstream from the mountain) is -0.0046 m s^{-1}, which is about 94% of the analytical value (-0.0049 m s^{-1}). Although about 60% of the computer time can be saved for the previous time-split simulation, the accuracy of the calculation is slightly sacrificed. For a very long integration, or waves very far from the energy source, the effect of the timesaving technique will show up.

6. Simulation of the 11 January 1972 Boulder windstorm

Our model was tested further in a non-linear situation. The non-linear effect in the flow over a 2-dimensional mountain contribute to the steepening of the mountain waves and may subsequently lead to wave breaking and severe downslope winds. The most well known observation of severe downslope winds is the 11 January 1972 Boulder windstorm (Lilly, 1978). The high wind speed and the nicely documented data generated interest in studying the phenomenon (Smith, 1985; Peltier and Clark, 1979; Durran, 1986; Durran and Klemp, 1987; Bacmeister and Pierrehumbert, 1988). In addition, a simulation of this case represented a challenging test to modelers due to the complex wave breaking structure and high wind speed. Recently, a collaborative effort was established to assess the ability of high-resolution numerical models to predict the location and strength of breaking waves in a series of experiments involving airflow over topography (Doyle et al., 2000). The first test of this joint effort was a multi-model inter-comparison of this particular windstorm. One of earlier versions of our numerical model joined the program. The

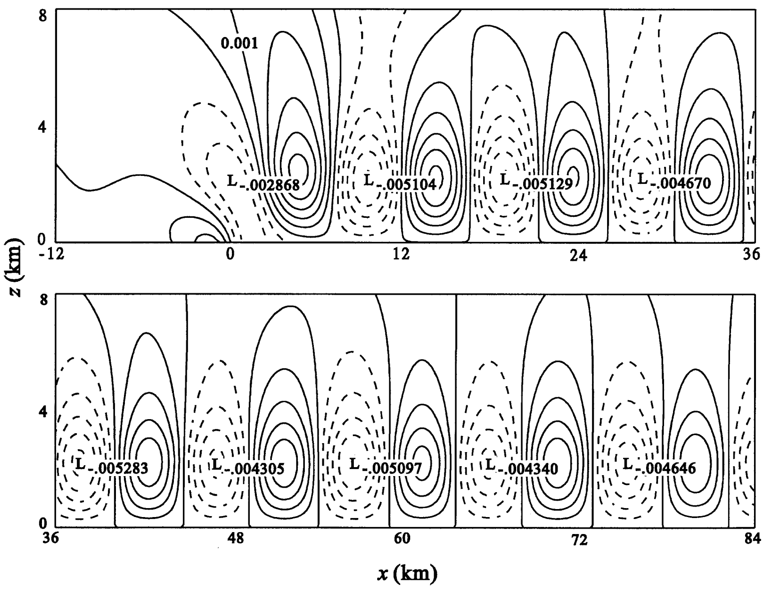

Fig. 10. Same as Fig. 8, except for numerical simulation without the time-split technique ($\Delta t = \Delta t_s = 0.5$ s).

results have shown consistency with the other models.

In this test, the initial conditions were based on the upstream 1200 UTC 11 January 1972 Grand Junction, Colorado sounding. The sounding profile is presented in Fig. 1 of Doyle et al. (2000). There were multiple shear layers with different amounts of static stability, which made the case even more interesting. Two of the most important features of this sounding profile were the strong wind and stable layers between 2 and 7 km. These characteristics favored the development of the windstorm (Klemp and Lilly, 1975; Durran, 1986). We spun up the horizontal wind in 10 min to avoid the initial shock waves generated by the high mountain from contaminating later model results. The idealized terrain height still followed a bell-shape with a half-width length of 10 km and a maximum height of 2 km. The grid intervals were 1 km in x and 200 m in z-direction. The integration domain was 370 km by 35 km in which the 50 km zone on both lateral boundaries and the top 10 km layer were sponge layers, where all prognostic variables were nudged toward their initial values to avoid wave reflection from the artificial boundaries. Time steps for the three different computational stages (Section 2) were 1/2, 1/2, and 4 s.

6.1. Model simulation after 2 h and comparison with observation

The simulated results after 2 h are shown in Fig. 11. The figure resembles the analysis of the observations in Figs. 7 and 9 of Lilly (1978). The contour-line intervals are the same in the two figures and only a portion of the simulated domain is shown for comparison. Major features of the phenomenon are well represented by the model. Upper-tropospheric isentropes are perturbed downward for more than 5 km and the entire tropospheric airflow plunged to a very thin layer over the downstream slope of the mountain. The simulated maximum wind speed is more than 60 m s^{-1} (Fig. 11b), which is about the same as the observed value (Lilly's Fig. 9). The "free fall" generated a "jump" analogous to a hydraulic jump found at the foot of a dam (Kundu, 1990; Durran, 1990). The jump is well defined in both figures. Farther downstream (to the right of the jump in the figure), the model catches the characteristic turbulent lee waves. The vertical amplitudes of the isentrope displacement of the lee waves are also quite comparable to the observation. In Lilly's Fig. 9, there is a narrow band located in the upper troposphere right above the zone with the severe downslope winds, where the horizontal wind was

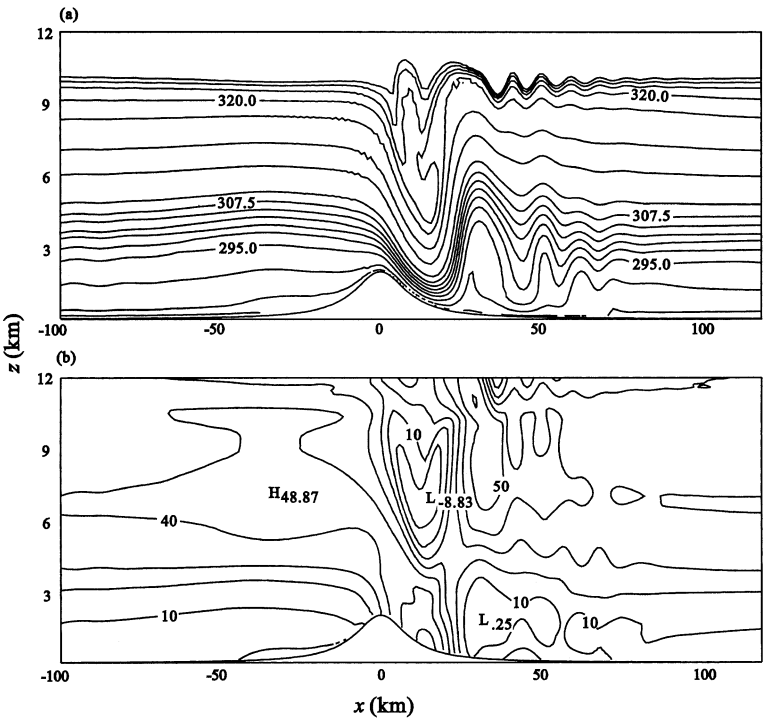

Fig. 11. (a) Potential temperature and (b) horizontal wind speed obtained by simulation of the 11 January 1972 windstorm after 2 h. Contour intervals are 2.5 K and 10 m s^{-1}, respectively.

very weak. The model also reproduced this important feature.

6.2. Model simulation after 3 h

The model results after 3 h are shown in Fig. 12. This is the time chosen by Doyle et al. (2000) for model performance intercomparison. There are many wave-breaking layers indicated by vertically oriented isentropes in Fig. 12a. This is partly due to the multiple layers of shear and stability residing in the initial sounding profile. The jump propagates downstream and the downslope wind speed upstream of the jump increases to 70 m s^{-1} (Fig. 12b). The low-level wind speed is most likely enhanced by a free-slip lower boundary. The areas of high wind speed and reversed airflow both elongated. They are stretched to the right along with the jump propagation. Another interesting characteristic is the strong wave motion in the layer right above the jump. This layer (between 10 and 12 km) is an inversion layer above the tropopause depicted by the densely distributed potential temperature contours. The jump apparently excites strong internal gravity waves, and part of the wave energy is trapped inside the inversion layer due to a near-neutral layer (between 12 and 14 km) just above the inversion. The trapped wave Scorer condition discussed in the previous section is met. It is noted that the near-neutral layer above the undulating inversion layer has been deepened by the second (from top) level of wave breaking over the mountain ridge, the potential temperature gradient of the inversion layer is therefore enhanced.

The vertical motion associated with the jump (Fig. 12c) is very strong. The magnitude and all features described in this subsection are quite consistent with the results of many other models presented in Doyle et al. (2000).

6.3. Sensitivity tests

The accuracy of the model was extensively tested for the time-split scheme, advection scheme, lateral boundary condition, and the spatial reso-

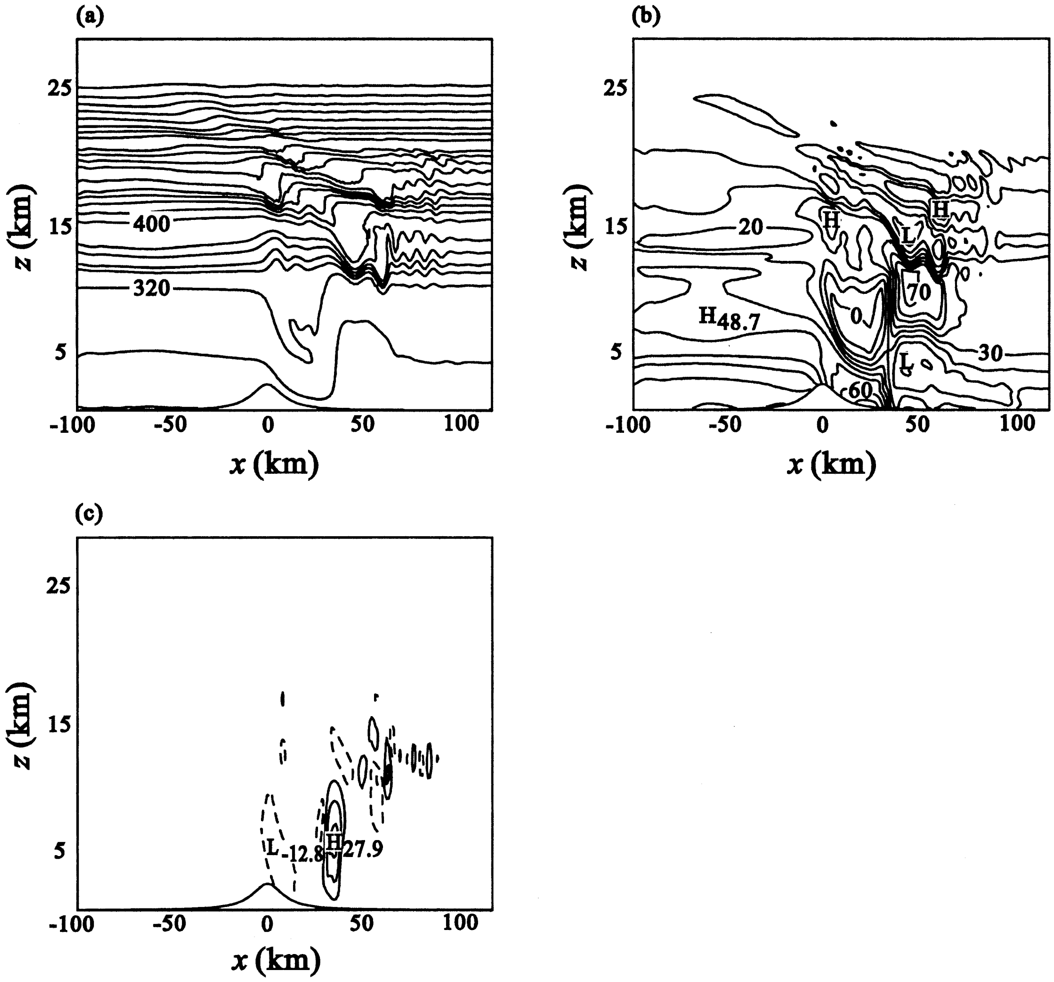

Fig. 12. Simulated (a) potential temperature, (b) horizontal wind speed and (c) vertical velocity after 3 h. Contour intervals for the 3 panels are 16 K, 10 m s^{-1}, and 10 m s^{-1}, respectively. The vertical velocity contours are -5, 5, and 15 m s^{-1} to avoid zero lines from dominating the figure and negative contours are dashed.

lution used in the model. Fig. 13 shows the 3-h model results of three other different simulations. Our time-split scheme, for $\Delta t = 3\,\Delta t_s$, seems to be valid as the results are quite similar with or without using the technique (compare panels Figs. 12a, 13a).

The model shows numerical solution robustness in terms of spatial resolution. Again, similar results were produced by simulations (panels (b) and (c) of Fig. 13) with half the horizontal and vertical grid spacing. A shorter time step is used to satisfy a more restrictive CFL criterion. The strength of the downslope wind is about the same, but the jump is sharper. The wavelength of the trapped waves discussed in Subsection 6.2 is shorter because of the stronger jump in the high-resolution tests.

Doyle et al. (2000) reported that although major features of the simulated downslope wind are similar for many numerical models, significant variations exist in the jump movement, the transition to ambient downstream conditions, and the vertical velocities. They suspect that some of these differences in the hydraulic behavior may be influenced by lateral boundary formulation. Our model results seem to be very robust in that respect as

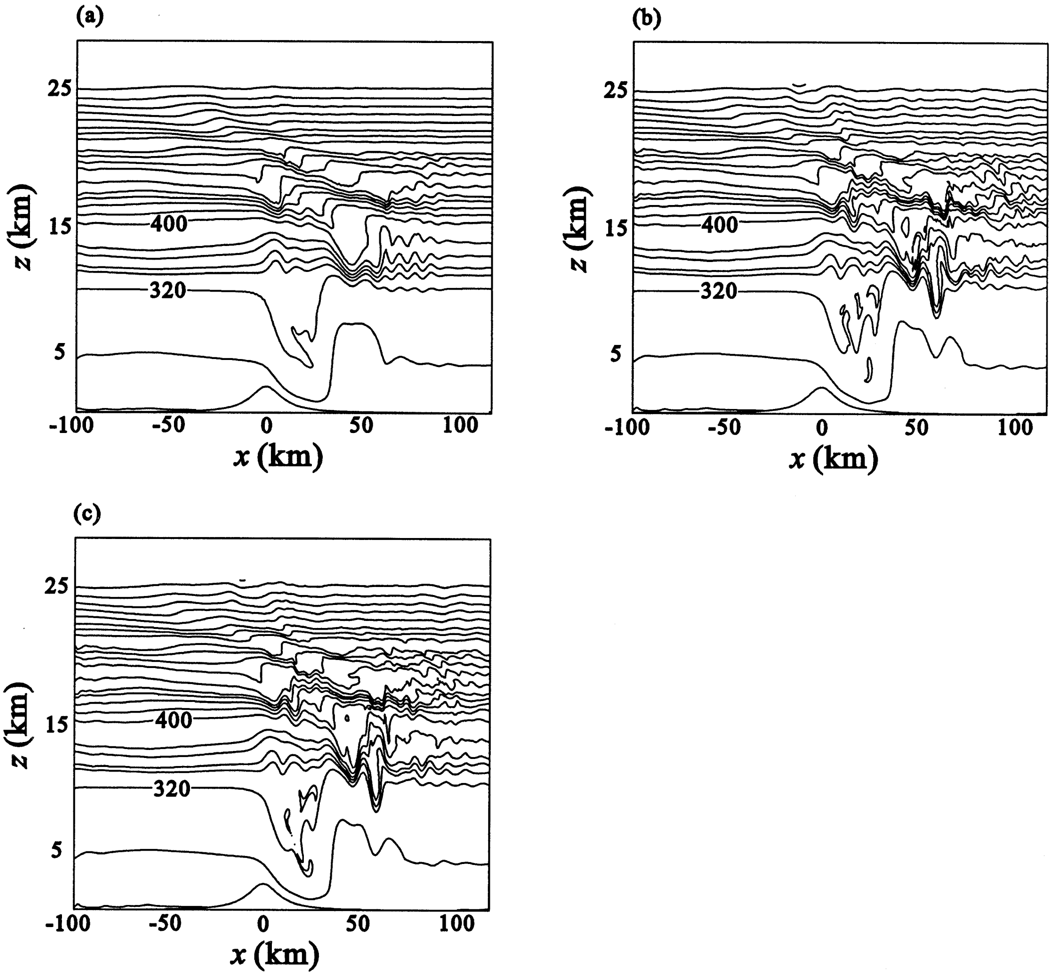

Fig. 13. Potential temperature after 3 h for different simulation cases. (a) Simulation using the same spatial resolution ($\Delta x = 1000$ m and $\Delta z = 200$ m) as in Fig. 12a but with time split technique $\Delta t = 3\ \Delta t_s$. Panels (b) and (c) for fine resolution ($\Delta x = 500$ m and $\Delta z = 100$ m) simulations. Panel (b) was obtained without the time-split technique and (c) with $\Delta t = 3\ \Delta t_s$. Contour interval (16 K) is the same for all plots.

well. We enlarged the buffer zone further by 50 points (50 km) on each side of the lateral boundary, and the results are practically the same as that of the smaller domain simulation. Since lateral boundaries are artificial boundaries, they should not have any impact on the simulated phenomenon. We also tested the effect of the accuracy of the horizontal advection scheme and found that the jump propagation is slower and the intensity of the phenomenon weaker if we used a 2nd order advection scheme instead of the present 4th order advection scheme. The major patterns (not shown in figures) for the two simulations are qualitatively similar.

The model is quite sensitive to the smoothing scheme for removing nonlinear instability. If we increase the smoothing coefficient or smooth too frequently, the whole system would be much weaker. Since the model is well-behaved, the amount of smoothing we used was minimal to avoid the artificial procedure from ruining the model results. The prognostic variables were smoothed every 30 s and the coefficient of Shuman smoothing was only 0.0125. This sensitivity test shows that the simulation of the windstorm is very demanding in terms of the accuracy and stability of a numerical model.

7. Bubble convection experiment

All of the tests in the previous sections are simulations for topographic flow. In this section, we show a flat-terrain bubble convection simulation. Robert (1993) presented a semi-implicit and semi-Langrangian method to simulate micro scale convective motion. His model is very efficient and accurate, but does not include the terrain effect and the paper describes convection only in an isentropic environment. We followed one of his experiments. The experiment involves a warm circular bubble in an isentropic environment. The initial distribution of potential temperature within the bubble is given by equations (38) and (39) in Robert (1993). This produces a bubble with a Gaussian profile. The diameter of the bubble is only 100 m and the maximum potential perturbation is 0.5 K in the center of the bubble. The grid interval is 10 m in both x and z directions as in Robert (1993). The time step that we used is very short with $\Delta t_b = 5\,\Delta t = 40\,\Delta t_s = 1$ s. Note that a large advection stage time step and high-frequency wave time step ratio can be used in a weakly stratified atmosphere, and there is no background stratification in this test. Another major difference is the domain size. We used a much larger domain (4 km × 4 km) than his (1 km in the x-direction and 1.5 km in height). As the bubble rises, the bubble becomes larger. The simulation result became sensitive to the lateral boundary condition at the later development of the convective motion when a small domain was used. In order to simulate unrestricted free motion and to avoid the problem with artificial lateral boundary conditions, we employed a very large calculating domain. The center of the bubble is 1 km above the bottom surface.

Our result at $t = 6$ min (not shown) is nearly identical to Robert's (1993) Fig. 4. Our 12th min result (Fig. 14a) is very similar to his Fig. 5, but the 18th min results are quite different (compare Fig. 14b and Robert's Fig. 6). The tail section of the rising bubble broke down at a later stage of integration (Fig. 14c) in our simulation. The difference in the 18 min result must be mainly due to the size of the integration domain. The convection motion at that time (Fig. 14d) is very strong at $x = -500$ and 500 m where Robert's lateral boundaries are located. The lateral boundary condition must have played a key role in the convective motion at that time in Robert's simulation. It may have accelerated the convective motion in his simulation and speeded up the break up process of the bubble. Chen (1999) simulated the same experiment with an implicit, multi-grid model. She has also used a large domain and her 18 min result is very close to ours.

This test shows that our finite difference model can achieve the same level of accuracy as a semi-Langrangian model as the two solutions were very close before the boundary effect sets in. Although there is no analytical solution for this non-linear situation, similar solutions by the three completely different models mentioned in the last paragraph should be sufficient to justify the numerical solution.

8. Summary and concluding remarks

In this paper we introduced a numerical model for solving a 2-dimensional, compressible, and nonhydrostatic system of equations. The new forward-backward procedure is neutral in time with respect to both sound waves and internal gravity waves in a linear sense. Compared to the leap-frog-scheme most people employ in their model, this method involves only two time steps, which requires less memory and is also free from computational modes. Hence, a time-filter is not needed. Pressure is retrieved from the predicted density field in the model. This method can be advantageous when diabatic effect is considered. In addition, treatment of the inviscid surface boundary condition is improved by manipulating the equations so that one-sided calculation for the vertical pressure derivative can be avoided. Since the treatment of the surface boundary condition is a 2nd order scheme as in the interior domain, this formulation contributes significantly to the performance of the model.

There are very few assumptions involved in solving the compressible, nonhydrostatic system of equations, and even sound waves are explicitly resolved. The integration time step is therefore very short. Fortunately, with the use of the time-

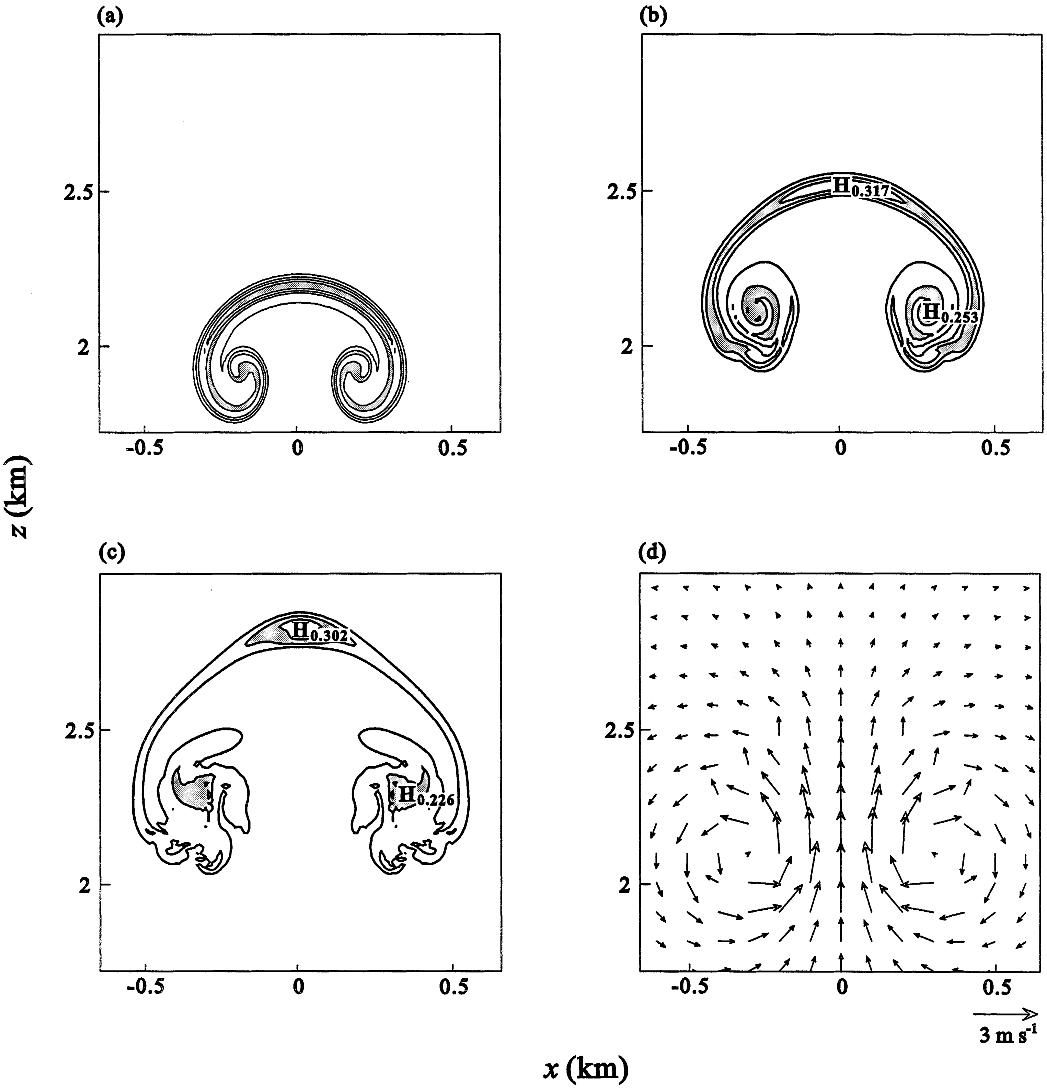

Fig. 14. Potential temperature perturbation at (a) 12 min, (b) 18 min, (c) 24 min, and (d) wind field at 18 min for an initially circular thermal bubble with a Gaussian profile in an isentropic environment. Contour levels for potential temperature perturbation are 0.05, 0.15, 0.25 and 0.35 K. Areas with value between 0.15 and 0.25 K, or greater than 0.35 K are shaded. The scale of the wind vectors is shown in the lower right corner of panel (d).

split technique described in Section 2 there are only a few terms that need to be calculated in the high-frequency-wave stage, while time-consuming advection terms can be calculated with a longer time step. The time-split technique seems quite valid as shown in all tests. Furthermore, even with a short time step, the numerical method is very stable in that this shortcoming does not pose any problems. The numerical results show no sign of deterioration for long integration. For example, the trapped waves of the 12-h result in Section 5 (Fig. 10) remains very strong very far downstrem from the mountain.

We have demonstrated the accuracy and stability of this model in both linear and nonlinear situations. We recalculated Queney's analytical solution for linear nonhydrostatic mountain waves through accurate numerical procedures with a very fine integration increment in order to validate our model. After redrawing the analytical solution, we found that our diagram is quite different from the original Queney's diagram. The result from our numerical model matches the recalculated solution very closely. Thus, the simulation further validates the recalculated solution. This practice also indicates that our numerical method is accurate.

In a nonlinear simulation of the 1972 Boulder windstorm, the model reproduced the intense windstorm. The results showed that the airflow is quasi-steady near the vicinity of the mountain and a "hydraulic jump" develops in the downstream region. Although there is no analytical solution for this complicated problem, the model result is at least very robust in terms of spatial resolution, lateral boundary conditions, and the use of time-split scheme even for this highly nonlinear and intense windstorm. The model result seems, therefore, credible.

This model will be converted into a 3-dimensional model to study many meso and micro scale phenomena. Currently, this model has also been applied to simulate nonlinear moist mountain waves, convective clouds, and land-sea breezes, etc.

9. Acknowledgments

This work has been jointly supported by National Science Council of Taiwan Grant NSC88-2111-M-002-013-AP3 and NSF Grant ATMS 9631572.

REFERENCES

Bacmeister, J. T. and Pierrehumbert, R. T. 1988. On high-drag states of nonlinear stratified flow over an obstacle. *J. Atmos. Sci.* **45**, 63–80.

Carpenter, K. M. 1979. An experimental forecast using a non-hydrostatic mesoscale model. *Quart. J. Roy. Meteor. Soc.* **105**, 629–655.

Chen, S. H. 1999. *The development of a nonhydrostatic model and a numerical study of flash flooding in the Ohio Valley*. PhD thesis. Department of Earth and Atmospheric Sciences, Purdue University, 181 pp.

Chern, J. D. 1994. *Numerical simulations of cyclogenesis over the western United States.* PhD thesis. Department of Earth and Atmospheric Sciences, Purdue University, 178 pp.

Clark, T. L. 1977. A small scale dynamical model using a terrain following coordinate transformation. *J. Comput. Phys.* **24**, 136–215.

Crowley, W. P. 1968. Numerical advection experiments. *Mon. Wea. Rev.* **96**, 1–11.

Cullen, M. J. P. 1990. A test of a semi-implicit integration technique for a fully compressible non-hydrostatic model. *Quart. J. Roy. Meteor. Soc.* **116**, 1253–1258.

Doyle, J. D., Durran, D. R., Chen, C., Colle, B. A., Georgelin, M., Grubisic, V., Hsu, W. R., Huang, C. Y., Landau, D., Lin, Y. L., Poulos, G. S., Sun, W. Y., Weber, D. B. Wurtele, M. G. and Xue, M. 2000. An intercomparison of model predicted wave breaking for the 11 January 1972 Boulder windstorm. *Mon. Wea. Rev.* **121**, 1493–1513.

Dudhia, J. 1993. A nonhydrostatic version of the Penn State–NCAR Mesoscale Model: Validation tests and simulation of an Atlantic cyclone and cold front. *Mon. Wea. Rev.* **128**, 901–914.

Durran, D. R. 1986. Another look at downslope windstorms. Part I: The development of analogs of supercritical flow in an infinitely deep, continuously stratified fluid. *J. Atmos. Sci.* **43**, 2527–2543.

Durran, D. R. 1990. Mountain waves and downslope winds. *Atmospheric process over complex terrain*, **23**. Blumen, W. (ed.). AMS, 59–81.

Durran, D. R. and Klemp, J. B. 1982. The effects of moisture on trapped mountain lee waves. *Mon. Wea. Rev.* **110**, 2490–2506.

Durran, D. R. and Klemp, J. B. 1983. A compressible model for the simulation of moist mountain waves. *Mon. Wea. Rev.* **111**, 2341–2361.

Durran, D. R. and Klemp, J. B. 1987. Another look at downslope windstorms. Part II: Nonlinear amplification beneath wave-overturning layers. *J. Atmos. Sci.* **44**, 3402–3412.

Gadd, A. J. 1978. A split explicit integration scheme for numerical weather prediction. *Quart. J. Roy. Meteor. Soc.* **104**, 569–582.

Gill, A. E. 1982. *Atmosphere-ocean dynamics.* Academic Press, New York, 662 pp.

Hodur, R. M. 1997. The Naval Research Laboratory Coupled Ocean/Atmosphere Mesoscale Prediction System (COAMPS). *Mon. Wea. Rev.* **125**, 1414–1430.

Hsu, W. R. and Sun, W. Y. 1994. A numerical study of a low-level jet and its accompanying secondary circulation in a Mei-Yu system. *Mon. Wea. Rev.* **122**, 324–340.

Ikawa, M. 1988. Comparison of some schemes for nonhydrostatic models with orography. *J. Meteor. Soc. Japan.* **66**, 753–776.

Klemp, J. B. and Lilly, D. K. 1975. The dynamics of wave-induced downslope winds. *J. Atmos. Sci.* **32**, 320–339.

Klemp, J. B. and Lilly, D. K. 1980. Mountain waves and momentum flux GARP Pub. Ser. 23. *Orographic effects in planetary flows*. ICSU/WMO, 450 pp.

Klemp, J. B. and Wilhelmson, R. 1978. The simulation of three-dimensional convective storm dynamics. *J. Atmos. Sci.* **35**, 1070–1096.

Kundu, P. K. 1990. *Fluid mechanics*. Academic Press, New York, 638 pp.

Lilly, D. K. 1978. A severe downslope windstorm and aircraft turbulence induced by a mountain wave. *J. Atmos. Sci.* **35**, 59–77.

Ogura, Y. and Phillips, N. A. 1962. Scale analysis of deep and shallow convection in the atmosphere. *J. Atmos. Sci.* **19**, 173–179.

Peltier, W. R. and Clark, T. L. 1979. The evolution and stability of finite-amplitude mountain waves. Part II: Surface drag and severe downslope windstorms. *J. Atmos. Sci.* **36**, 1498–1529.

Pielke, R. A., Cotton, W. R., Walko, R. L., Tremback, C. J., Lyons, W. A., Grasso, L. D., Nicholls, M. E., Moran, M. D., Wesley, D. A., Lee, T. J. and Copeland, J. H. 1992. A comprehensive meteorological modeling system — RAMS, *Meteor. Atmos. Phys.* **49**, 69–91.

Pinty, J.-P., Benoit, R., Richard, E. and Laprise, R. 1995. Simple tests of a semi-implicit semi-Lagrangian model on 2D mountain wave problems. *Mon. Wea. Rev.* **123**, 3042–3058.

Queney, P. 1948. The problem of airflow over mountains: A summary of theoretical studies. *Bull. Amer. Meteor. Soc.* **29**, 16–26.

Robert, A. 1993. Bubble convection experiments with a semi-implict formulation of the Euler equations. *J. Atmos. Sci.* **50**, 1865–1873.

Scorer, R. S. 1949. Theory of waves in the lee of mountains. *Quart. J. Roy. Meteor. Soc.* **75**, 41–56.

Skamarock W. C. and Klemp, J. B. 1992. The stability of time-split numerical methods for the hydrostatic and the nonhydrostatic elastic equations. *Mon. Wea. Rev.* **120**, 2109–2127.

Smith, R. B. 1979. The influence of mountains on the atmosphere. In: *Advances in Geophysics*, vol. **21** (B. Saltzman ed.), pp. 87–230. Academic Press.

Smith, R. B. 1985. On severe downslope winds. *J. Atmos. Sci.* **42**, 2597–2603.

Smolarkiewicz, P. K. and Margolin, L. G. 1997. On forward-in-time differencing for fluids: An Eulerian/semi-Lagrangian nonhydrostatic model for stratified flows. *Atmos.-Ocean* **35**, 127–152.

Steppeler, J. 1995. Comments on "A nonhydrostatic version of the Penn State–NCAR Mesoscale Model: Validation tests and simulations of an Atlantic cyclone and cold front." *Mon. Wea. Rev.* **123**, 2572.

Sun, W. Y. 1980. A forward-backward time integration scheme to treat internal gravity waves. *Mon. Wea. Rev.* **108**, 402–407.

Sun, W. Y. 1993. Numerical experiment for advection equation. *J. Comput. Physics.* **108**, 264–271.

Sun, W. Y. and Hsu, W. R. 1988. Numerical study of cold air outbreak over the warm ocean. *J. Atmos. Sci.* **45**, 1205–1227.

Sun, W. Y., Cherm, J. D., Wu. C. C. and Hsu, W. R. 1991. Numerical simulation of mesoscale circulation in Taiwan and surrounding area. *Mon. Wea. Rev.* **119**, 2558–2573.

Tanquay, M., Robert, A. and Laprise, R. 1990. A semi-implicit semi-Lagrangian full compressible regional forecast model. *Mon. Wea. Rev.* **118**, 1970–1980.

Tapp, M. C. and White, P. W. 1976. A non-hydrostatic mesoscale model. *Quart. J. Roy. Meteor. Soc.* **102**, 277–296.